PHYSICAL REVIEW D **73,** 104002 (2006)

Binary black hole merger dynamics and waveforms

John G. Baker,[1] Joan Centrella,[1] Dae-Il Choi,[1,2] Michael Koppitz,[1] and James van Meter[1]

[1]*Gravitational Astrophysics Laboratory, NASA Goddard Space Flight Center, 8800 Greenbelt Rd., Greenbelt, Maryland 20771, USA*

[2]*Universities Space Research Association, 10211 Wincopin Circle, Suite 500, Columbia, Maryland 21044, USA*

(Received 9 February 2006; published 2 May 2006)

We study dynamics and radiation generation in the last few orbits and merger of a binary black hole system, applying recently developed techniques for simulations of moving black holes. Our analysis of the gravitational radiation waveforms and dynamical black hole trajectories produces a consistent picture for a set of simulations with black holes beginning on circular-orbit trajectories at a variety of initial separations. We find profound agreement at the level of 1% among the simulations for the last orbit, merger and ringdown. We are confident that this part of our waveform result accurately represents the predictions from Einstein's General Relativity for the final burst of gravitational radiation resulting from the merger of an astrophysical system of equal-mass nonspinning black holes. The simulations result in a final black hole with spin parameter $a/m = 0.69$. We also find good agreement at a level of roughly 10% for the radiation generated in the preceding few orbits.

DOI: 10.1103/PhysRevD.73.104002 PACS numbers: 04.25.Dm, 04.30.Db, 04.70.Bw, 95.30.Sf

I. INTRODUCTION

Two black holes in a binary system spiral together due to the emission of gravitational waves. The final merger stage of a binary in which the black holes have comparable masses will produce a spectacular burst of gravitational radiation and is expected to be one of the brightest sources in the gravitational wave sky. Mergers of binaries containing two stellar black holes are important targets for the first-generation LIGO gravitational wave detectors, now operating at design sensitivity in a year-long science data-taking run, as well as other ground-based detectors such as VIRGO and GEO. Knowledge of the waveforms from the final merger phase is important to improve the detectability of these sources by such detectors [1,2]. Mergers of massive black hole binaries are important sources for the space-based LISA, currently in the formulation phase. Since LISA is expected to observe these massive black hole mergers at relatively high signal-to-noise ratios [3], comparison of the data with calculated merger waveforms should allow a test of General Relativity in the dynamical, nonlinear regime.

In the early stages of the binary inspiral, the black holes are widely separated and the waveforms can be calculated analytically using perturbative methods. However, waveforms from the final merger, in which the black holes plunge together and form a single, highly-distorted black hole with a common horizon, demand full 3-D numerical relativity simulations of the full Einstein equations. This proved be a very difficult undertaking and, for roughly the past decade, 3-D numerical relativity simulations have been beset by pernicious numerical instabililties that prevented the simulation codes from running long enough to evolve any significant fraction of a binary orbit.

Recently, however, dramatic progress has been made in evolving the merger of equal-mass binary black holes. Using excision to remove the singular regions within the horizons and a corotating coordinate system to keep the black holes fixed in the numerical grid, a binary has been evolved through a little more than an orbit, and through merger [4–6], though without being able to extract gravitational waves. Simulations of excised black holes allowed to move through the grid on one or more orbits and then through merger have been carried out, with the extraction of gravitational radiation [7]. In addition, new techniques allowing the black holes to move without the need for excision have been developed independently by the authors of this paper and another research group [8,9]; these have been applied to study the final plunge, and merger of a binary, with the calculation of gravitational waves. Recently, these techniques have been applied to evolve a binary with nonequal masses [10] and the last orbit and merger of an equal-mass binary [11]. It is especially noteworthy that this progress is occurring on a broad front, by several independent groups using different techniques.

Several major open questions in the area of binary black hole mergers center on the dependence of the resulting gravitational waveforms on the initial data. In order to use numerical relativity simulations to compare with data from gravitational wave detectors, we need to model astrophysically realistic binary black hole configurations. For nonspinning equal-mass black holes, how strongly do the gravitational waveforms for the merger depend on the initial data? What are the effects of spin and nonequal masses on the resulting waveforms? The answers to such questions can only be approached using an evolutionary analysis, in which different initial data sets are evolved and the resulting waveforms are compared.

In this paper, we take a step towards answering these questions by evolving several initial data sets for nonspinning equal-mass black holes through the final few orbits, plunge, merger and ringdown. To accomplish this, we apply our new methods that allow puncture black holes to move freely across a grid. Using adaptive mesh refine-

ment, we can resolve the dynamical regions near the black holes (having length scales $\sim M$, where M is the total mass of the system and we use $c = G = 1$) and the outer regions where the gravitational waves are extracted (having length scales $\sim(10\text{–}100)M$). Putting the outer boundary typically at $t \approx 768M$, causally disconnected from the dynamical regions and wavezone throughout most of the simulation, we can evolve stably for $t > 800M$. The initial data sets are chosen to be puncture data [12].

Our study focuses on simulations beginning from a set of four inspiralling black hole configurations modeled as described in Sec. II and using techniques discussed in Sec. III. In Sec. IV we calibrate the performance of our numerical techniques with a resolution study of simulations from the configuration with the shortest initial separation. Our main results are presented in Sec. V where we comparatively study the radiation waveforms and black hole trajectories. We find a close relationship between the trajectory information and the waveforms, providing a consistent picture of the black hole dynamics. The radiation from the final orbit, merger and ringdown agrees to high precision among the runs from our range of initial configurations, with the runs from the farthest initial separation producing a promising waveform approximately through the last three orbits

II. INITIAL DATA

We start by setting up initial data for equal-mass binary black holes represented as ''punctures'' [12]. The metric on the initial spacelike slice is written in the form $g_{ij} = \psi^4 \delta_{ij}$, where $i, j = 1, 2, 3$, with conformal factor $\psi = \psi_{\rm BL} + u$. The static, singular part of the conformal factor takes the form $\psi_{\rm BL} = 1 + \sum_{n=1}^{2} m_n/2|\vec{r} - \vec{r}_n|$, where the nth black hole has mass m_n and is located at coordinate position $\vec{r}_n$. The nonsingular function u is calculated by solving the Hamiltonian constraint equation using `AMRMG` [13].

The punctures are initially placed on the y-axis in the equatorial ($z = 0$) plane. We need to specify the individual puncture mass m, coordinate position Y, and momentum P so that the black holes are on approximately circular orbits and have no individual spins (they are irrotational). To accomplish this, we follow the prescription for estimating quasicircular initial data from the QC sequence given in Ref. [14]. These data are based on values of P/M_0 and Y/M_0 determined by Cook ([15]; see also [16]), who uses an effective potential method that minimizes the binary system energy while holding the orbital angular momentum fixed, to produce an approximately circular orbit. Our values for Y and P differ slightly from those in Ref. [14] because we have more precisely determined the value of M_0 in setting up the data.

The parameters and physical quantities for the simulations we ran are shown in Table I. Here, Y is the initial coordinate position of each puncture along the y-axis, P is the linear momentum of an individual puncture, and m is the mass of the puncture. M_0 is the initial total ADM mass of the binary and J_0 is the initial total angular momentum. L is the initial proper separation of the black holes, approximated by $L = \int_{H_1}^{H_2} \sqrt{g_{yy}} dy$, where each limit H_i represents a point on the Schwarzschild horizon associated with mass m_i at position $\vec{r}_i$.

TABLE I. Initial data parameters and physical quantities for the runs considered in this paper.

Run	$\pm Y$	$\pm P$	m	M_0	J_0	L/M_0
R1	3.257	0.133	0.483	0.996	0.868	9.9
R2	3.776	0.119	0.488	1.001	0.899	11.1
R3	4.251	0.109	0.49	1.002	0.928	12.1
R4	4.77	0.101	0.492	1.003	0.959	13.2

We note that our runs R1, R2, R3, and R4 correspond closely to the initial data for models QC-6, QC-7, QC-8, and QC-9, respectively, along the QC sequence. As shown in Ref. [14], at these relatively wide initial separations, the parameters for these initial data sets are close to those derived using post-Newtonian (PN) techniques; see, in particular, Figs. 26–28 in Ref. [14].

III. SIMULATION TECHNIQUES

We evolve the initial data with the `Hahndol` code [17], which uses a conformal (BSSN) formulation of Einstein's evolution equations on a cell-centered numerical grid. The basic equations are the same as given in Ref. [17], with the exception that the evolution equation for the BSSN variable $\tilde{\Gamma}^i$ has been modified for stability as suggested in [18]. In addition, to reduce high frequency noise associated with refinement interfaces, we add some dissipation of the form given in [19].

Mesh refinement and parallelization are implemented in our code with the `PARAMESH` package [20,21]. We use 4th-order centered differencing for the spatial derivatives except for the advection of the shift, which is performed with 4th-order upwinded differencing. The refinement boundary interfaces are buffered with 4th-order-interpolated guard cells which, at worst, may introduce 2nd-order errors into second derivatives. With our current mesh refinement implementation, our accuracy is limited by spatial finite differencing error from refinement interfaces. Since we do not gain much by using higher order time integration, we use 2nd-order time stepping via a three-step iterative Crank-Nicholson scheme. Even though, overall, we expect 2nd-order convergence, we have found considerable advantage in using 4th-order spatial differencing over 2nd-order spatial differencing, as measured by the accuracy and manifest convergence of the Hamiltonian constraint and other quantities.

Traditionally, puncture black holes have been evolved by keeping them fixed in the grid [4,5]. This is accomplished by factoring out the singular part $\psi_{\rm BL}$ and handling

it analytically, while evolving only the regular parts of the metric. As explained in detail in [8], we employ instead newly developed techniques that allow the puncture black holes to move freely across the numerical grid. The singular part is not factored out; instead the entire conformal factor is evolved. Initially, the binary is set up so that the centers of the punctures are not located at grid points (as in the traditional implementation). Taking numerical derivatives of $\psi_{\rm BL}$ causes an effective regularization of the puncture singularity through the inherent smoothing of finite differences.

Our new approach allows the punctures to move freely by implementing a modified version of the Gamma-driver shift vector [22]. The Gamma-driver condition generally improves numerical stability by evolving the coordinates towards quiescence, in accord with the physical dynamics. Our modification to this gauge is tailored for moving punctures, as mentioned in [8]. Specifically we use

$$\partial_t \beta^i = \frac{3}{4}\alpha B^i \tag{1}$$

and

$$\partial_t B^i = \partial_t \tilde{\Gamma}^i - \beta^j \partial_j \tilde{\Gamma}^i - \eta B^i \tag{2}$$

for the shift β^i and

$$\partial_t \alpha = -2\alpha K + \beta^i \partial_i \alpha \tag{3}$$

for the lapse α. The lapse Eq. (3) is the well-known "1 + log" slicing condition, modified with an advection term as in [9]. We use the initial gauge conditions $\beta = 0$, $B = 0$, and $\alpha = \psi^{-2}$, similar to those recommended in [9]. We place the punctures in the $z = 0$ plane and impose equatorial symmetry throughout.

We use adaptive mesh refinement to produce a numerical grid having appropriate resolution in the strong-field dynamical regions near the black holes and in the wave zone. Initially, we set up the black hole binary in a numerical domain with a box-in-box refinement structure having an innermost refinement of h_f and subsequent boxes of twice that resolution. We start with two boxes centered on each individual black hole, and then a box centered on the origin that encompasses both black holes. Subsequent boxes centered on the origin are used to give up to a total of 10 refinement levels.

During the evolution the black holes move freely across the grid, changing the curvature in the surrounding region; in response, the initial grid structure is changed adaptively. Paramesh works on logically Cartesian, or structured, grids and carries out the mesh refinement on grid blocks. If the curvature reaches a certain threshold (a free parameter in our code) at one point of a block, that block is bisected in each coordinate direction to produce 8 child blocks, each having half the resolution of the parent block. If all points in all the child blocks fall below the threshold, those blocks get derefined.

The box stretching from $-48M$ to $+48M$ in the x- and y-directions and from 0 to $+48M$ in the z-direction is fixed in place throughout all runs.[1] Boxes inside this one can, and generally do, change adaptively as the simulation evolves; boxes outside this one maintain their original locations on the grid. At the initial time, there is a box stretching out to $24M$; as the binary evolves, this box generally shrinks as the black holes spiral in towards the center. The resolution in the region between this box and the next (fixed) one at $\pm 48M$ is $h_w = 32h_f$ in all runs. We generally extract gravitational waves on a sphere of radius $r_{\rm ex} = 30M$. In the early stages of the run, this sphere intersects the next innermost box with resolution $h_w/2$; at later times, it is completely located within the region having resolution h_w.

We extract gravitational waves from our simulations using the Weyl tensor component Ψ_4. Our wave extraction techniques are based on Misner's method [23] and are 2nd-order accurate. They are robust and accurate even when the extraction radii cross mesh refinement boundaries [24]. In particular, the waveforms computed at various extraction radii $r_{\rm ex}$ are preserved up to the leading order $1/r$ scaling and show no ill effects from passing through one or more refinement boundaries.

IV. CALIBRATION OF SIMULATIONS

We have performed detailed studies of the errors and convergence behavior of simulations run on the `Hahndol` code using fixed mesh refinement in previous work [8,17,24,25]. The simulations presented here differ from this earlier work in two important ways: they are carried out using an adaptive mesh structure that changes as the binaries evolve, and they are run for significantly longer durations. In this section, we discuss the calibration tests we have carried out to verify that the code produces robust, reliable results in these more challenging regimes.

We performed these calibration tests on run R1, which we ran at three different resolutions. The initial data parameters for R1 are given in Table I and the simulation parameters for these three cases are shown in Table II. We use a base resolution of $\rho = 3M/32 = 0.09375M$ from which we reach the three resolutions used in the runs. Note that the medium resolution case, $h_f = \rho/3$, has the outer boundary located relatively close, at $\pm 192M$; this was one of the earliest runs we did. Since the simulation runs for a total duration $T_{\rm sim} = 332M$, small errors from this outer boundary do have time to propagate in to the physically interesting regions of the grid. While these effects are generally small and have no significant impact on the dynamics or wave extraction, we did use a more distant outer boundary at $\pm 768M$ in all other runs to eliminate this

[1]For convenience, we use $M = 1$ to set the scale for the computational grid and time. Note that the actual initial total ADM mass for each case is $M_0 \approx M$, as given in Table I.

TABLE II. Parameters for the low, medium, and high resolution runs of model R1, where $\rho = 3M/32 = 0.09375M$. $T_{\rm sim}$ is the total duration of the simulation.

R1 cases	low	medium	high
h_f	$\rho/2$	$\rho/3$	$\rho/4$
outer boundary	$\pm 768M$	$\pm 192M$	$\pm 768M$
$T_{\rm sim}$	$186M$	$332M$	$291M$

problem. This adds only a small overhead to the overall cost of the simulation, due to the fixed mesh refinement structure used in the outer regions.

For these three runs, we scaled the criterion for refinement and derefinement to provide as closely as possible the same grid structure at the same physical time in the simulations. Since it is generally not possible to match the grid structures exactly, pointwise convergence tests are of questionable value. Instead, we calculated the $L1$ norm of the Hamiltonian constraint C_H over the grid as a function of time. This norm was taken over all levels inside the box at $\pm 48M$, which includes the wave extraction zone. Figure 1 shows the $L1$ norms for these three runs; note that the initial growth of the constraint violation is brought to a halt after approximately $50M$ of evolution and then diminishes. We attribute this behavior in C_H to a gauge wave pulse that we have observed leaving the source region early in the simulation. The gauge wave has strong high frequency components and is thus prone to generating differencing error and reflections from refinement boundaries. C_H settles down somewhat after the gauge wave leaves the grid, as suggested by the plot. The curves are scaled so that, for 2nd-order convergence, they would lie on top of each other. As Fig. 1 shows, we get 2nd-order convergence (or slightly better) for the entire course of the run.

The gravitational waves are extracted on a sphere of radius $r_{\rm ex} = 30M$. The top panel of Fig. 2 shows the $l = 2$, $m = 2$ component of $r\Psi_4$ for the three different resolution runs, where r is the estimated areal radius of the extraction sphere [24]. The waves start out in phase; note, in particular, the agreement in the initial pulse around $t \sim 30M$. However, as the runs proceed, timing differences slowly accumulate over the relatively long orbital time scales. By $t \sim 150M$, significant differences have accumulated in the lowest resolution case (solid line) compared to the other two runs; we attribute this to the larger inherent numerical diffusion in this lowest resolution run.

A naive convergence test, in which we take differences directly between the waveforms at the same simulation times, is shown in the bottom panel of Fig. 2; these curves are scaled so that, for 2nd-order convergence they would coincide. Comparing the top and bottom panels, it is clear that the differences between these curves can mainly be attributed to the differences in the phases of the waveforms. At several times, the phases are actually off by π so that the differences between the two waves is twice as large as the individual waves themselves.

A more meaningful convergence test is shown in Fig. 3. Here, we have shifted the waveforms in time and phase to adjust for the timing differences using the techniques

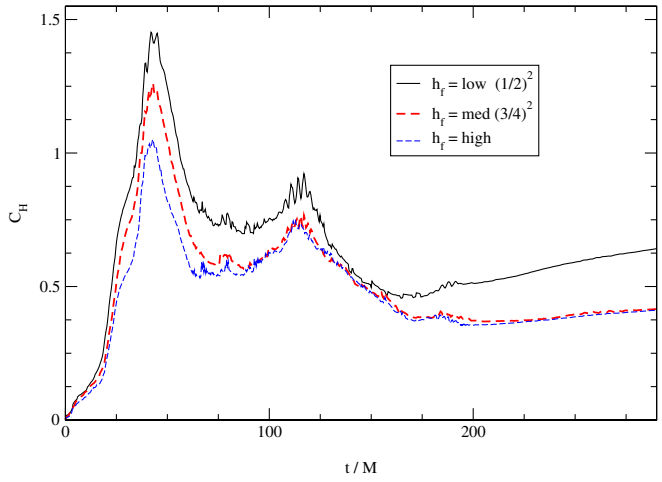

FIG. 1 (color online). The $L1$ norm of the Hamiltonian constraint violation is shown as a function of time for the three different resolution runs of R1 given in Table II. The high resolution case is shown with a dashed line. The medium (bold dashes) and low (solid) cases are scaled so that, for 2nd-order convergence all three curves would lie on top of each other. The $L1$ norm is taken over all levels of the grid inside $48M$, including the wave extraction region. This figure indicates satisfactory convergence of the Hamiltonian constraint error in our simulations.

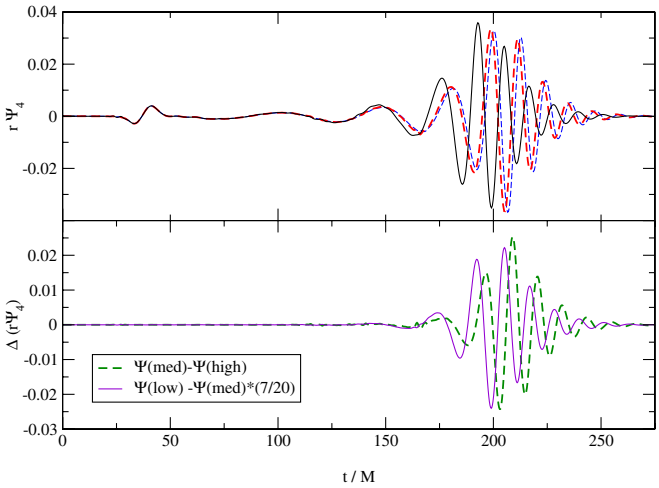

FIG. 2 (color online). Gravitational waveforms and a naive convergence test. The top panel shows the $l = 2$, $m = 2$ mode of Ψ_4 for the low (solid), medium (bold dashes), and high (dashes) resolution runs of R1. The lower panel shows the differences between these waveforms; for 2nd-order convergence, the curves would lie on top of each other. Phase differences between the waveforms account for the large differences shown. When the phases are shifted appropriately, the convergence of the waves is more manifest, as in Fig. 3.

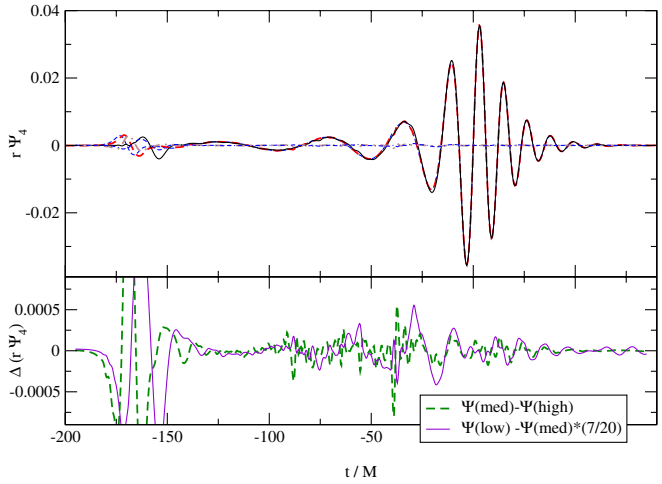

FIG. 3 (color online). Time-shifted gravitational waveforms and a physical convergence test. The labels in the top panel are as in Fig. 2. In the top panel, the gravitational waveforms have been shifted in time so that the peak amplitude of the radiation occurs at $t = 0$. The differences between these time-shifted waveforms are shown in the bottom panel; these curves are scaled so that they would lie on top of each other for 2nd-order convergence.

described below. The time axis has been relabeled so that the peak of the radiation occurs at $t = 0$. The top panel shows the $l = 2$, $m = 2$ mode of $r\Psi_4$ for the low (solid), medium (bold dashes), and high (dashes) resolution cases; note that the physical parts of the waveforms ($t \gtrsim -125M$) agree beautifully. We then carried out a convergence test using these shifted curves; the results are shown in the bottom panel. Again, the curves are scaled so to lie on top of each other for 2nd-order convergence. Here we see nearly perfect convergence for the physical parts of the waveforms; note, in particular, the much smaller vertical scale in the lower panel of Fig. 3.

As we discussed in [8], the gravitational waveforms can be used to calculate the total energy $E_{\rm rad}$ and total angular momentum $J_{\rm rad}$ carried away by the radiation. We calculate dE/dt and dJ/dt from time integrals of all $l = 2$ and $l = 3$ waveform components using Eqs. (5.1) and (5.2) in [14]. Integrating dE/dt gives the total energy loss due to the radiation, $E_{\rm rad}$. We find that the influence of higher modes of the waves contributes $<1\%$ to the energy and even less to the angular momentum.

The total radiated energies calculated from the waveforms extracted at different radii and with different resolutions are reported in Table III. For lower resolution, the radiated energy depends somewhat on the extraction radius, decreasing with increasing radius. For the medium and high resolution cases, however, the values are almost independent of the extraction radius. This indicates that the further out, lesser refined regions of the grid produce significant dissipation of the waves in the low resolution case, whereas when the resolution is high enough, the lesser refined regions do not have such an effect. These considerations indicate that the best radius to extract the energy is at $r_{\rm ex} = 30M$, in a region refined enough that the energy does not significantly dissipate in the low resolution run, yet far enough way from the source that it changes only minimally for higher resolution runs.

TABLE III. Values of the energy $E_{\rm rad}$ (in units of M_0) and angular momentum $J_{\rm rad}$ (in units of M_0^2) carried away by gravitational radiation for the R1 runs calculated for different extraction radii and different resolutions.

h_f		$r_{\rm ex} = 20M$	$r_{\rm ex} = 30M$	$r_{\rm ex} = 40M$	$r_{\rm ex} = 50M$
$\rho/2$	$E_{\rm rad}$	0.0347	0.0343	0.0336	0.0324
	$J_{\rm rad}$	0.217	0.218	0.218	0.215
$\rho/3$	$E_{\rm rad}$	0.0343	0.0345	0.0345	0.0343
	$J_{\rm rad}$	0.215	0.223	0.226	0.227
$\rho/4$	$E_{\rm rad}$	0.0342	0.0344	0.0345	0.0344
	$J_{\rm rad}$	0.216	0.224	0.227	0.228

As shown in Table III, the radiated angular momentum $J_{\rm rad}$ varies by a few percent between $r_{\rm ex} = 30M$ and $r_{\rm ex} = 50M$ at high resolution. This observation seems to agree with the notion that the angular momentum depends more strongly on the longer wavelength parts of the waves [14], which should be extracted at greater distances. For all the runs reported in this paper, we use an extraction radius of $r_{\rm ex} = 50M$ to calculate $J_{\rm rad}$.

V. RESULTS

In this section we comparatively analyze the results of simulations based on our R1–R4 black hole configurations. Recall that the initial data for each of these simulations starts the black holes at different separations, with proper separations varying from $9.9M_0$ to $13.2M_0$, and provided with sufficient angular momentum that the runs are estimated to be on initially circular orbits.

We can think of each of these simulations as an approximate representation of the late-time portion of an ideal spacetime which begins with arbitrarily well-separated black holes on an inspiraling trajectory which asymptotically approaches circular orbits. As such representations, there are several limitations which the initial data models may have. In particular, the initial parameters will only approximate the ideal trajectory since the angular momentum as a function of radius may differ from the value required for an idealized circular orbit. Likewise, at finite radius, the ideal spiral trajectory can only be approximated by our initially circular configurations.

Furthermore the manner by which we have mapped from these trajectory specifications to actual initial data values necessarily requires making some suppositions. For instance, our puncture data prescription, like almost all field prescriptions, contains no representation of prior radiation generated before the time at which the initial data are

posed. Though it is generally expected that the significance of such limitations on the final merger simulations should be reduced if the black holes begin sufficiently far apart, there is no clear way to assess just how significant such effects will be on the results, including the gravitational waveforms, before carrying out the evolutions.

Our simulations, begun with varying initial separations, should be affected by any initial modeling error in varying amounts, but should agree to the degree that they represent the ideal astrophysical spacetime. A key objective in our analysis is to identify *universal* characteristics among the different runs which, we reason, are then likely to correctly represent those aspects of the astrophysical equal-mass nonspinning binary black hole merger spacetime.

A. Overview of simulations

Our comparative analysis covers four simulations labeled R1 to R4 in Table I. We evolved them all using the medium resolution of $h_f = \rho/3$ except for R1, where we have applied the higher $h_f = \rho/4$ resolution. In all runs we used an initial grid setup and adaptive mesh refinement as described in Sec. III. We evolved all the runs to well after the wave signal had passed the extraction region; the actual amount of time is noted as $T_{\rm sim}$ in Table IV. For the time-slicing condition used in our simulations, the region where the lapse satisfies the condition $\alpha = 0.3$ corresponds roughly with the apparent horizon location. We thus used the moment when the two $\alpha = 0.3$ regions around the black holes merge to specify a merger time $T_{\rm merge}$. The number of orbits for each run, $N_{\rm orbits}$, was estimated from the trajectories shown in Fig. 4 and is taken up to the point at which the merger occurs.

A graphical overview of our four simulations is presented in Fig. 4 showing the paths traced by the black hole punctures on the computational domain. These were obtained by numerically integrating the equation of motion $\dot{\vec{x}}_{\rm punc} = -\vec{\beta}(\vec{x}_{\rm punc})$, which analytically gives the exact trajectory of each puncture [9]. The value of the shift at the location of the puncture $\vec{\beta}(\vec{x}_{\rm punc})$ was interpolated between grid points as required.

For clarity, Fig. 4 shows only the track of one of the two black holes from each simulation. We have oriented each trajectory according to a physical reference discussed in Sec. V B, so that they superpose at the radiation peak, which occurs very near the end of the puncture trajectory. R4 has the widest initial separation and completes the largest number of orbits. Each of the other cases, after an

TABLE IV. Simulation parameters and general results. $T_{\rm merger}$ is the time at which the merger occurs, starting from the initial time in each run.

	R1	R2	R3	R4
L/M_0	9.9	11.1	12.1	13.2
h_f	$\rho/4$	$\rho/3$	$\rho/3$	$\rho/3$
$T_{\rm sim}$	$421M$	$531M$	$530M$	$850M$
$T_{\rm merger}$	$160M$	$234M$	$396M$	$513M$
$N_{\rm orbits}$	1.8	2.5	3.6	4.2

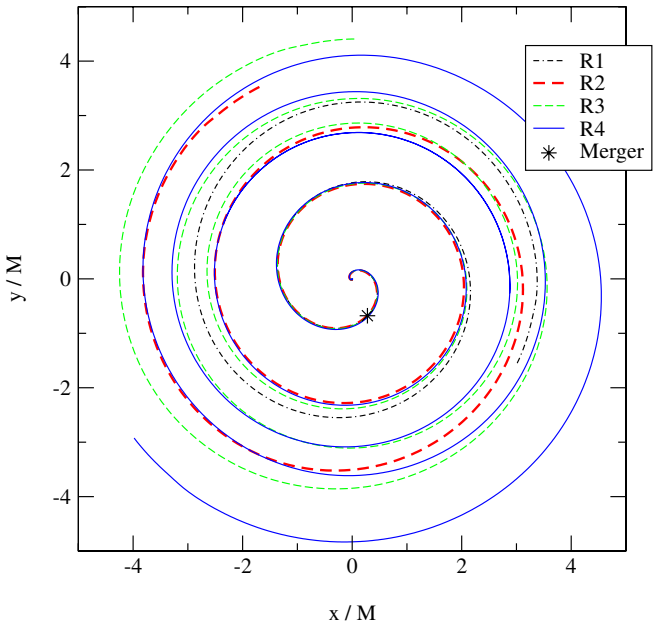

FIG. 4 (color online). Paths of black holes starting from different initial separations. For clarity, we show only the track of one of the black holes from each simulation. The paths are very similar for approximately the last orbit, indicating that the black holes follow the same tracks. The point of merger (estimated by a single connected isosurface of $\alpha = 0.3$) is indicated by an asterisk in the plot.

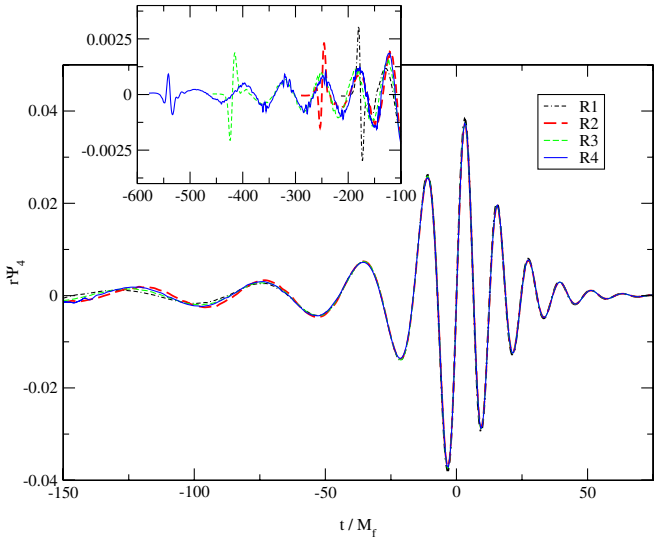

FIG. 5 (color online). Waveforms from runs R1–R4. The figure shows nearly perfect agreement after $t = -50M_f$. For the preceding $500M_f$, shown in an inset, the waveforms agree in phase and amplitude within about 10% except for a brief initial pulse at the beginning of each run.

initial transient period of approximately one orbit, nearly locks on to the R4 trajectory. For the final orbit, all four trajectories are very nearly superposed. In Sec. V C we study the quantitative features of these trajectories in more detail.

Figure 5 shows one polarization component of $r\Psi_4$ for the runs R1–R4, extracted at $r_{\rm ex} = 30M$ and shifted in time and phase as described below. Notice that beyond about $t = -50M_f$ the waveforms superpose sufficiently well that it is not possible to distinguish the curves in the plot. The very strong agreement among our simulations on this part of the wave gives us confidence that our waveforms accurately represent the astrophysical merger-ringdown signal to high precision. The inset shows that the agreement remains generally good going back to the beginning of each simulation, with the R3 and R4 runs agreeing fairly well over some $450M_f$.

B. Gravitational radiation

The first step in quantitatively comparing our runs is to calculate the energy and angular momentum carried away by the gravitational radiation generated by the binary system in our simulations. Following the discussion in Sec. IV, we measure the radiation energy extracted at $r_{\rm ex} = 30M$, estimating that these will be accurate within $\sim 1\%$. We subtract the radiation energy $E_{\rm rad}$ from the initial mass M_0, given in Table I, to determine the final black hole mass in each simulation, $M_f = M_0 - E_{\rm rad}$. This provides a physical scaling which we use to compare the R1–R4 simulations. Similarly, we measure the angular momentum content of the radiation $J_{\rm rad}$ as extracted at $r_{\rm ex} = 50M$, estimating the accuracy to be within a few percent. Subtracting this from the initial ADM angular momentum J_0, we calculate the spin parameter of the final black hole $a/M_f = (J_0 - J_{\rm rad})/M_f^2$. The results are summarized in Table V.

We note that the energy and angular momentum content of the radiation is almost entirely contained in the $l = 2$, $m = \pm 2$ spin -2-weighted spherical harmonic components, with other components entering at the 1% level. In the remainder of our waveform analysis we concentrate exclusively on the leading component,

$$r\psi_4(\theta, \varphi) \sim r\Psi_{4(22)}({}_{-2}Y_{22}(\theta, \phi) + {}_{-2}Y_{2-2}(\theta, \phi)) \quad (4)$$

where, for simplicity, we have suppressed retarded time dependence. Hereafter we suppress the multipole labels and refer to the leading component simply as $r\Psi_4$. The two polarization components of the radiation are represented in the real and imaginary parts of $r\Psi_4$. We follow Refs. [14,26], representing our waveforms by $r\Psi_4 = A\exp(-i\varphi_{\rm pol})$, where the amplitude A and polarization phase $\varphi_{\rm pol}$, like $r\Psi_4$, are functions of time. Of course, any complex time-series could be represented in this form, but it is particularly valuable if the radiation exhibits a *circular polarization* pattern, so that A and $\varphi_{\rm pol}$ vary slowly compared to the wave frequency timescale. Such radiation will be circularly polarized to an observer on the system's rotational axis, varying to linearly polarization for an observer on the equatorial plane. We find that the radiation produced in our simulations shows strong circular polarization, which we will utilize in comparing the radiation from our four simulations.

As we are interested in the degree to which our various runs may be taken to be different models of the same physical merger spacetime, we must define a physical basis for comparing them. As expected, runs beginning with more separated black holes take a longer time to reach the point of merger. For each run, a physical reference time is recognizable by the point at which the radiation reaches its peak amplitude; we define $t = 0$ at this point for our comparisons.

Figure 6 shows the wave amplitudes $A(t)$ from all four runs. Through the strong radiation peak after $t = -50M_f$ all four wave amplitudes show striking universality in the compared results, with agreement among all runs to about 1%. This period of strong agreement covers roughly the

TABLE V. Energy and angular momenta for the radiation and final black hole. $E_{\rm rad}$ and $J_{\rm rad}$ are measured at $r_{\rm ex} = 30M$, and $r_{\rm ex} = 50M$, respectively. $M_{\rm QN}$ and $a_{\rm QN}$ are calculated independently from the quasinormal fits of the ringdown waveforms, and agree well with the values deduced from the radiative losses.

	$E_{\rm rad}/M_f$	$J_{\rm rad}/M_f^2$	a/M_f	$M_{\rm QN}/M_f$	$a_{\rm QN}/M_f$
R1	0.0356	0.246	0.694	1.005	0.721
R2	0.0369	0.272	0.691	1.002	0.686
R3	0.0381	0.306	0.689	1.004	0.694
R4	0.0387	0.325	0.702	1.004	0.693

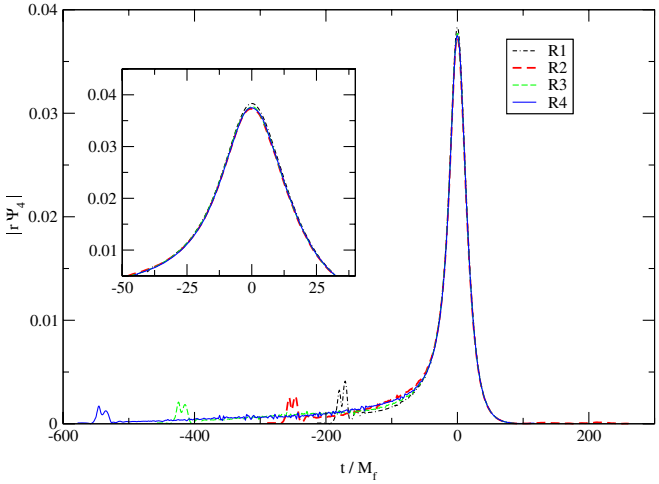

FIG. 6 (color online). Amplitudes, absolute values of (complex) Ψ_4, of the waves. The curves have been shifted such that the maxima are all at time 0. The inset zooms into the peak showing the strong agreement from $t = -50M_f$ on. We have used the amplitude peak as a reference to align our simulations in time.

last orbit, plunge and ringdown of the merger. Agreement within about 10% is maintained among the R2–R4 simulations for most of each run with slightly more difference in the R1 run. The smooth shape of the peak, lacking any sign of the several wave cycles spanning the peak (see Fig. 5) is an indication of the circular polarization pattern discussed above. The only clearly nonuniversal feature in the wave amplitudes is a small and brief burst lasting about $50M_f$ at the beginning of each run. We interpret this burst as "spurious radiation" content in the initial data. As generally expected the amplitude of the spurious radiation lessens as the initial separation of the black holes is increased.

Since the black holes in our various runs (which all begin on the y-axis) undertake differing amounts of orbital motion before merger, we must expect differing orientations for the systems at the point of merger. For meaningful comparisons we must rotate the data from each system to align them with respect to some physical reference. As our reference, we will orient the systems so that the polarization phase $\varphi_{\rm pol}$ of the radiation passes though zero at the moment of peak amplitude $t = 0$. We use this orientation for all figures with wave phase information, and in the trajectory comparison in Fig. 4.

The polarization phase $\varphi_{\rm pol}$ is shown in Fig. 7. At time $t = 0M_f$ the phases are set to agree. However, they keep agreeing after that, showing that the ring-down frequency is the same. The plot shows generally good phase agreement among all runs, to within a small fraction of a wave cycle, except for a brief period at the beginning of each run when the radiation is dominated by spurious radiation associated with initial data modeling error, and is not circularly polarized. For circularly polarized radiation it is meaningful to define an instantaneous frequency for the

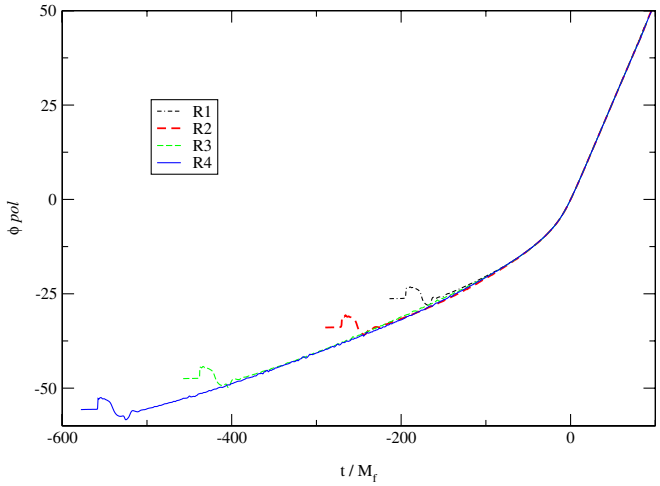

FIG. 7 (color online). Graviational wave phase angle vs time. The phase is made to agree at time $t = 0M_f$. After $t = -50M_f$ the phases agree very well for all the runs. For the duration of the runs (except for a brief initial period), the waveforms from all runs agree in phase within about 10% of a wave cycle.

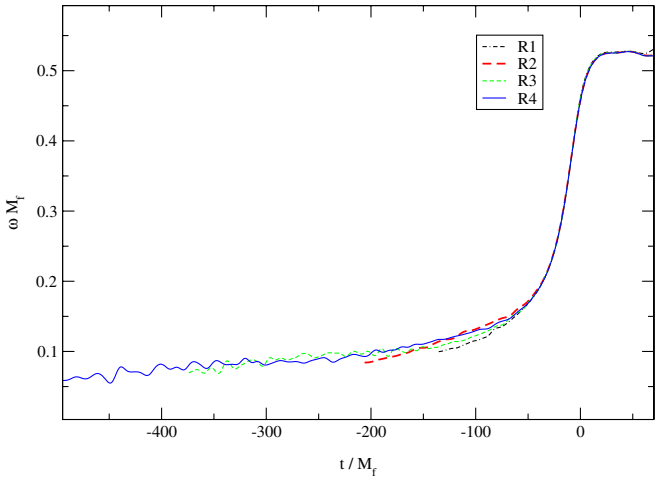

FIG. 8 (color online). Waveform frequency as a function of time. The curves are nearly indistinguishable after $t = -50M_f$.

wave, $\omega = \partial\varphi_{\rm pol}/\partial t$, shown in Fig. 8, which allows a more detailed comparison of the simulation waveforms. It can be seen that apart from the noise due to the smallness of the waves initially and at the end, all runs have the same frequency evolution from about $60M_f$ before the merger. Before that the frequency evolution compares similarly among the simulations with some wavyness which may correspond to some ellipticity in the early part of each simulation's insprial.

The final (constant) frequency is the frequency of the ringdown. Fitting an exponential decay to the amplitudes and using this final frequency we estimate, using the procedure in Ref. [27], the mass and angular momentum of the black hole formed in the merger. These estimates provide a description of the final black hole as determined by its perturbative dynamics. The results are listed in Table V, where they can be compared with the independent estimates obtained by subtracting the radiation losses from the initial values. The good agreement, to 1–2%, provides a measure of energy and angular momentum conservation in each simulation. We also note the strong agreement among our simulations (which start from different separations) on the final state of the remnant black hole, with the measures from the R2–R4 runs consistent with the same value, $a/M_f = 0.69(\pm 1\%)$. The R1 value differs by a few percent, which may be a consequence of the shorter duration of this simulation, allowing greater sensitivity to initial transient effects.

C. Trajectory analysis

In this section we consider the particlelike dynamics of our simulations defined by the coordinate trajectories of our black hole punctures. It is important to be careful in interpreting such coordinate-dependent information which may include nonphysical gauge features. Nonetheless it is worth noting that the Gamma-driver gauge condition ap-

plied in our simulations, to the extent that it approximates $\tilde{\Gamma}^i = \tilde{\gamma}^{ij}_{,j} = 0$, is similar to the Dirac gauge applied in some post-Newtonian calculations, and might be expected to provide a sensible coordinate system at least in weak-field regions. In any case, since we apply similar coordinate conditions in each run, the coordinate-based puncture trajectories provide another opportunity to identify universal features in our simulations that start from different initial separations.

Refer again to Fig. 4, which shows the tracks of one of the punctures from each of the runs R1–R4 as they spiral into the center. As the black holes descend deeper into the strong field, we see that their paths lock on to a universal trajectory that takes them into the plunge and subsequent merger. This behavior can also be seen in Fig. 9, which shows the coordinate separation between the punctures as a function of time. In this case, there is strong agreement among the runs after $t \approx -50M_f$. In the earlier part of the simulations there are clear differences among the runs, which are suggestive of ellipticity in the initial orbital motion.

One way to estimate the utility of such coordinate information is by comparison with our much more invariant waveform data. We can, for instance, compare the coordinate orbital frequency Ω with the waveform frequency examined above. With suitable coordinates, in the weak-field limit, we would expect the orbital frequency to be approximately equal to half the gravitational wave frequency. In Fig. 10 we compare the coordinate orbital frequency Ω with half the gravitational wave frequency from our R4 run. We find that, if we shift the orbital freqency data by about $33M_0$, the two curves match very well. Despite some noise in our wave frequency, most features in the orbital frequency are tracked in the wave

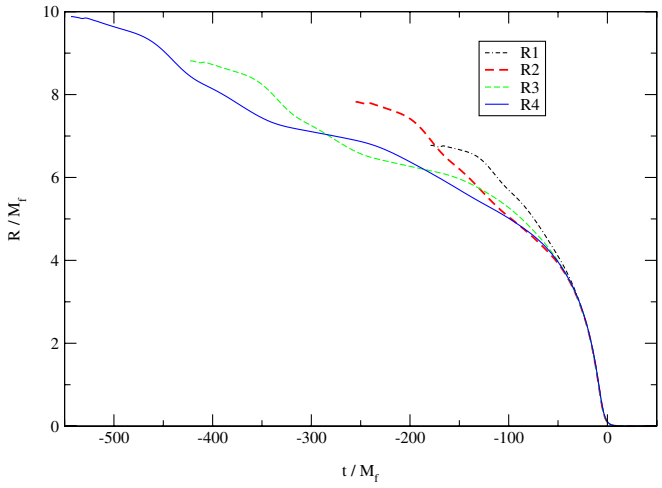

FIG. 9 (color online). The coordinate separation between the punctures is shown for runs R1–R4 as a function of time. Early on in each simulation the separation seems to drop quickly, but all runs track together as they approach merger.

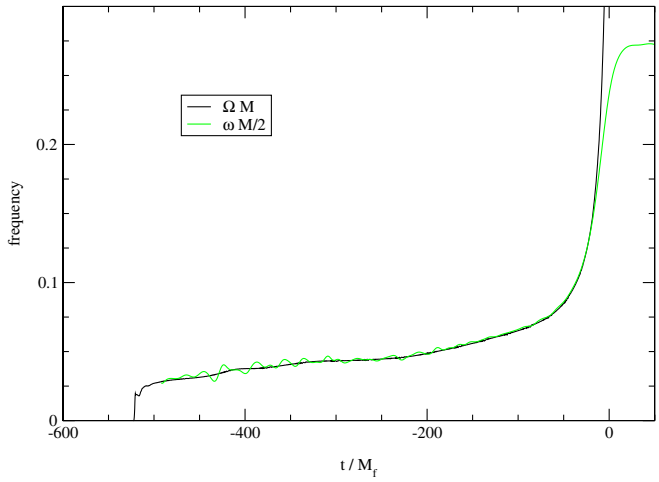

FIG. 10 (color online). Orbital and radiation frequencies for R4. We show the evolution of the orbital frequency Ω, calculated from the coordinate motion of the punctures, compared with the wave frequency. The good correspondence motivates a closer examination of the coordinate-based puncture trajectories. (Note that the radiation frequency is divided by two since $\omega = 2\Omega$).

frequency as well. Exceptions occur at the very beginning of the simulation, where our coordinates necessarily start with the punctures nonmoving (hence $\Omega = 0$) before the brief period through which the coordinate puncture velocities seem to adapt well to the physical dynamics. Likewise, at late times, we see that the orbital puncture frequency continues to grow while the radiation frequency saturates at the quasinormal ringing frequency. This seems to correspond to the expectation that, at late times, the coordinate motion of the punctures decouples from the process of radiation generation, with the punctures continuing to fall into the newly formed black hole while gravitational ring-down radiation is generated in the final black hole's pertubative potential barrier region somewhat outside the horizon.

The $33M_0$ time shift required to realize this agreement can be interpreted as the time required for the gravitational radiation to propagate out to the point where it is extracted at $r_{\rm ex} = 30M$. We can utilize this time correspondence to roughly associate phenomena occurring in the strong field region of the simulations with features in the radiation. We have used this time-shift to compare the time at which peak radiation is generated in our simulations with $T_{\rm merge}$ in Table IV. In our simulations, we find that the merger occurs about $12M$ before the radiation peak is generated.

In Fig. 11 we compare the orbital frequencies of the puncture trajectories among our R1–R4 runs. As was the case with the wave frequencies we see excellent agreement among the runs after $t = -50M_f$. Here we have focused on the earlier region where the results are not quite as universal. In each run we notice that after a period of initial angular acceleration the orbital frequencies agree to within a few percent. This initial transient period is at least

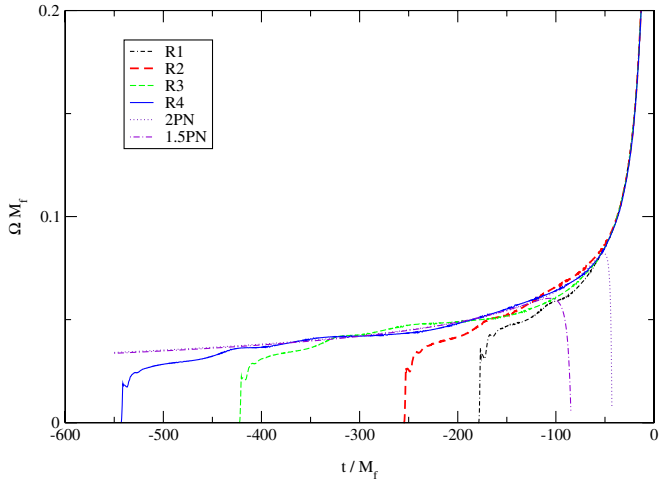

FIG. 11 (color online). The frequencies as functions of time. Shown are frequencies calculated from the puncture trajectories showing the agreement of the different runs and two curves calculated using Post-Newtonian approximations.

partially a coordinate effect (since Ω must begin at 0), but the strong similarity with the wave-frequencies suggests that there may be a physical basis for the descrepancies as well. Particularly for R3 and R4, the shape of the curves suggests a slow oscillation, perhaps some ellipticity in the motion. For an external comparison, we have included the post-Newtonian frequency evolution 1.5PN and 2PN order, as provided in Ref. [28], positioned in time so that all curves agree near $t = -200M_f$. The correspondence with these PN curves is certainly striking, though we caution that the 2.5PN curve does not agree so well, with its peak frequency topping out too low for a useful comparison here. In subsequent work we intend to explore comparisons with post-Newtonian calculations in more detail.

VI. DISCUSSION

We have presented a set of numerical simulations representing the last few orbits and merger of an equal-mass nonspinning binary black hole system. Though the initial data differ, with the black holes starting out at separations ranging from $9M$ to $13M$, the calculated waveforms are dominated by universal characteristics. Over the period beginning from about $50M$ before the gravitational wave peak, and covering approximately the last orbit, all our simulations show profound agreement, with differences among the waveforms at no more than about 1%. The robustness of this part of our waveform is strong evidence that it accurately represents the final burst of gravitational radiation from an astrophysical system of equal-mass, nonspinning black holes, as predicted by Einstein's field equations.

We also see good agreement among our simulations in the gravitational radiation generated in the several preceding orbits which we have simulated. Excepting an initial transient period about $100M$ for each run, the earlier portion of the waveforms show good agreement, within approximately 10% in phasing and amplitude. For our longest simulation (R4) this suggests that we have produced a good approximation of the astrophysical waveform prediction covering more than $400M$ before the radiation peak. We are further encouraged by good agreement over much of this period among the frequency evolution of our simulated waveforms (especially R4), with the second-order (2PN) post-Newtonian predictions. We are currently exploring the correspondence of our waveforms with post-Newtonian calculations, to be developed in more detail in a future publication.

That the late-time part of the simulations (the final orbit and thereafter) shows stronger universality than the earlier part of the simulations supports idea that the late dynamics of the system is dominated by the strong interaction of the holes, and radiative losses, which have the effect of reducing dependence on prior conditions. For the remnant black hole formed in the merger, our simulations consistently predict a spin within about 1% of $a/m = 0.69$.

Our simulations have employed newly developed numerical relativity techniques for evolving black holes, which allows the black holes to propagate accurately across the numerical domain [8,9]. This approach does not require excision of the black hole interior from the computational domain. We have calibrated our approach on one of our black hole configurations, R1, demonstrating 2nd-order convergence, and waveform accuracy at the 1% level in the last orbit. For all our simulations we have found good energy and angular momentum conservation as measured by comparing the mass and spin of the final black hole, measured by its quasinormal ringing, with the expected remainder after radiative losses. In future work we expect to continue to refine our techniques for accuracy and efficiency over long-lasting simulations.

Our results can be compared to Refs. [5,11], which each recently presented simulations of inspiraling mergers from initial data with separation $9.3M$, slightly closer than our $9.9M$ R1 case. They agreed on a merger time of about $125M$, consistently less than the $160M$ for R1. Ref. [11] goes on to determine a waveform for the peak portion of the radiation which appears to be similar to our robustly determined final radiation burst, while finding a value of $a/m \sim 0.68$ for the spin of the final black hole, quite close to our result.

We have also studied the trajectories traced out by the motion of the black holes in our numerical coordinate system. These trajectories suggest a coherent picture of the system's evolution which is qualitatively, and in some ways, quantitatively consistent with invariant information measured in the radiation waveforms. This correspondence provides some foundation for giving a tentative physical interpretation to some coordinate-based information in our simulations, such as the number and rate of inspiral orbits,

and recommends further research toward a deeper understanding of the properties of the coordinate systems which we have applied in these simulations.

Our comparative analysis provides some insight into the quality of the initial data models which we have applied. We have seen an indication of a small amount (with negligible energy content) of spurious radiation arising from initial modeling error. As generally expected the scale of this spurious radiation decreases for increasingly well-separated initial data. For sufficiently long-lasting runs this spurious radiation is well-segregated in time, limiting its direct significance in interpreting the merger radiation. Of perhaps greater concern are indications which suggest ellipticity in the inspiral trajectories and waveforms. Two aspects of our initial data model may be contributing to this effect. First, there will be some level of mismatch between the initial separation of the black holes and the specified initial value of angular momentum. We comment, in this regard, that other simulations we have looked at in preparation for the work presented here hint that the early transient part of each simulation, as well as measures such as the merger times, may depend sensitively on small (1%) changes in the initial angular momentum. Secondly, as is customary, the data we have applied have the black holes set on initially circular trajectories, with vanishing radial momentum components. This may also be expected to lead to ellipticity, as has been noted in binary neutron star simulations [29]. We expect to explore these and similar concerns in future simulations.

Taken together with other recent progress in numerical relativity, these results herald a new age of numerical simulations applied to further characterize and understand strong-field binary black hole interactions and merger radiation. Future applications will begin to explore the physical parameter space of these systems to study, particularly, the effect on the radiation waveforms of individual black hole spin, and variations in the black hole mass ratio.

ACKNOWLEDGMENTS

We thank David Brown for providing `AMRMG`, and Cole Miller for many insightful discussions. This work was supported in part by NASA grants No. ATP02-0043-0056 and O5-BEFS-05-0044. The simulations were carried out using Project Columbia at NASA Ames Research Center, and at the NASA Center for Computational Sciences at Goddard Space Flight Center. M. K. and J. v. M. were supported by the Research Associateship Programs Office of the National Research Council and the NASA Postdoctoral Program at the Oakridge Associated Universities.

[1] A. Buonanno and T. Damour, Phys. Rev. D **62**, 064015 (2000).
[2] T. Damour, B. R. Iyer, and B. S. Sathyaprakash, Phys. Rev. D **62**, 084036 (2000).
[3] Éanna É. Flanagan and S. A. Hughes, Phys. Rev. D **57**, 4535 (1998).
[4] M. Alcubierre *et al.*, Phys. Rev. D **72**, 044004 (2005).
[5] P. Diener *et al.*, Phys. Rev. Lett. **96**, 121101 (2006).
[6] B. Bruegmann, W. Tichy, and N. Jansen, Phys. Rev. Lett. **92**, 211101 (2004).
[7] F. Pretorius, Phys. Rev. Lett. **95**, 121101 (2005).
[8] J. G. Baker, J. Centrella, D.-I. Choi, M. Koppitz, and J. van Meter, Phys. Rev. Lett. **96**, 111102 (2006).
[9] M. Campanelli, C. O. Lousto, P. Marronetti, and Y. Zlochower, Phys. Rev. Lett. **96**, 111101 (2006).
[10] F. Herrmann, D. Shoemaker, and P. Laguna, gr-qc/0601026.
[11] M. Campanelli, C. O. Lousto, and Y. Zlochower, Phys. Rev. D **73**, 061501 (2006)..
[12] S. Brandt and B. Brügmann, Phys. Rev. Lett. **78**, 3606 (1997).
[13] J. D. Brown and L. L. Lowe, J. Comput. Phys. **209**, 582 (2005).
[14] J. Baker, M. Campanelli, C. O. Lousto, and R. Takahashi, Phys. Rev. D **65**, 124012 (2002).
[15] G. B. Cook, Phys. Rev. D **50**, 5025 (1994).
[16] T. W. Baumgarte, Phys. Rev. D **62**, 024018 (2000).
[17] B. Imbiriba *et al.*, Phys. Rev. D **70**, 124025 (2004).
[18] H.-J. Yo, T. Baumgarte, and S. Shapiro, Phys. Rev. D **66**, 084026 (2002).
[19] E. Schnetter, S. H. Hawley, and I. Hawke, Class. Quant. Grav. **21**, 1465 (2004).
[20] P. MacNeice, K. Olson, C. Mobarry, R. de Fainchtein, and C. Packer, Comput. Phys. Commun. **126**, 330 (2000).
[21] http://ct.gsfc.nasa.gov/paramesh/Users_manual/amr.html.
[22] M. Alcubierre, B. Brügmann, P. Diener, M. Koppitz, D. Pollney, E. Seidel, and R. Takahashi, Phys. Rev. D **67**, 084023 (2003).
[23] C. W. Misner, Class. Quant. Grav. **21**, S243 (2004).
[24] D. R. Fiske, J. G. Baker, J. R. van Meter, D.-I. Choi, and J. M. Centrella, Phys. Rev. D **71**, 104036 (2005).
[25] D.-I. Choi, J. D. Brown, B. Imbiriba, J. Centrella, and P. MacNeice, J. Comput. Phys. **193**, 398 (2004).
[26] J. Baker, M. Campanelli, C. O. Lousto, and R. Takahashi, Phys. Rev. D **69**, 027505 (2004).
[27] E. W. Leaver, Proc. R. Soc. A **402** (1986).
[28] L. Blanchet, Living Rev. Relativity **5**, 3 (2002).
[29] M. Miller, Phys. Rev. D **69**, 124013 (2004).